Phase saturation control on mixing-driven reactions in 3D porous media

Markale, Ishaan; Cimmarusti, Gabriele M; Britton, Melanie M; Jiménez-Martínez, Joaquín

DOI:
10.1021/acs.est.1c01288

Document Version
Publisher's PDF, also known as Version of record

Citation for published version (Harvard):
Markale, I, Cimmarusti, GM, Britton, MM & Jiménez-Martínez, J 2021, 'Phase saturation control on mixing-driven reactions in 3D porous media', *Environmental Science and Technology*, vol. 55, no. 13, pp. 8742-8752. https://doi.org/10.1021/acs.est.1c01288

Environmental Science & Technology

pubs.acs.org/est

Article

Phase Saturation Control on Mixing-Driven Reactions in 3D Porous Media

Ishaan Markale, Gabriele M. Cimmarusti, Melanie M. Britton, and Joaquín Jiménez-Martínez*

Cite This: *Environ. Sci. Technol.* 2021, 55, 8742–8752

Read Online

ACCESS | Metrics & More | Article Recommendations | Supporting Information

ABSTRACT: Transported chemical reactions in unsaturated porous media are relevant to environmental and industrial applications. Continuum scale models are based on equivalent parameters derived from analogy with saturated conditions and cannot appropriately account for incomplete mixing. It is also unclear how the third dimension controls mixing and reactions. We obtain three-dimensional (3D) images by magnetic resonance imaging using an immiscible nonwetting liquid as a second phase and a fast irreversible bimolecular reaction. We study the impact of phase saturation on the dynamics of mixing and the reaction front. We quantify the temporally resolved effective reaction rate and describe it using the lamellar theory of mixing, which explains faster than Fickian ($t^{0.5}$) rate of product formation by accounting for the deformation of the mixing interface between the two reacting fluids. For a given Péclet, although stretching and folding of the reactive front enhance as saturation decreases, enhancing the product formation, the product formation is larger as saturation increases. After breakthrough, the extinction of the reaction takes longer as saturation decreases because of the larger nonmixed volume behind the front. These results are the basis for a general model to better predict reactive transport in unsaturated porous media not achievable by the current continuum paradigm.

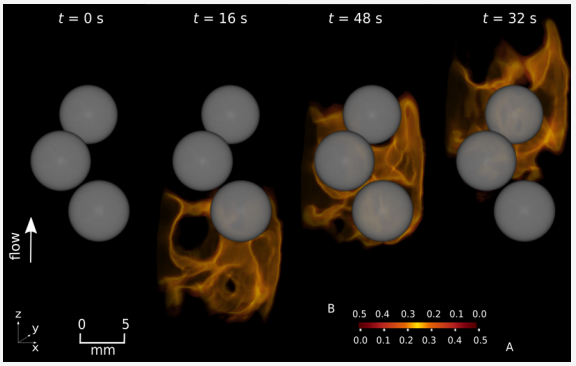

KEYWORDS: *pore-scale reaction, incomplete mixing, magnetic resonance imaging, reactive lamella model, reaction extinction*

1. INTRODUCTION

The chemical and biological evolution of many natural, engineering, and industrial systems is governed by reactive mixing interfaces.[1−4] Chemical reactions in the fluid are driven by mixing, which is a process that brings together segregated substances. Mixing is primarily driven by stretching, due to the existence of fluid velocity gradients, and diffusion.[5−7] Porous media are topologically complex environments with highly heterogeneous fluid flow dynamics. Under unsaturated conditions, i.e., in the presence within the pore space of another phase such as an immiscible liquid or gas, this is exacerbated by a much more complex spatial configuration of the phases. This affects the internal connectivity of the system,[8] further increasing the fluid flow heterogeneity with the formation of preferential paths (high-velocity zones) and stagnation zones (low-velocity zones). Understanding mixing and reactions in unsaturated flows in porous media is fundamental to predicting the dynamics of contaminants and evaluating the role of the soils in controlling global carbon, i.e., soil respiration,[9−11] nitrogen,[12−14] and trace element[15] cycles. It is also key as it plays a major role in applications such as catalytic reactors,[16] contaminant (bio)remediation,[17] enhanced oil recovery,[18] and nuclear waste disposal.[19]

The classic modeling approaches, also called Fickian or dispersive-diffusive, for reactive transport in unsaturated conditions are often based on equivalent parameters (e.g., dispersion) derived from analogy with saturated conditions, with systematic ad hoc incorporation of saturation dependency (fraction of the pore volume occupied by one of the immiscible phases).[20] Fundamentally, these models cannot predict accurately the kinetics of transported reactions resulting from mixing, which intrinsically occur at the pore scale.[17,21] Stretching and folding of reactive fronts by the high flow heterogeneity enhance mixing and thus reaction compared to diffusive mixing only.[22−24] Recently developed lamellar mixing models that couple stretching and diffusion to capture the pore-scale concentration fluctuations are a promising avenue to predict reactive processes in these highly complex systems.[25−27]

Mixing and reactive transport at the pore scale have been studied experimentally using two-dimensional (2D) milli- and microfluidic approaches in saturated and unsaturated conditions.[28−31] Various numerical studies have further added

Received: February 25, 2021
Revised: May 28, 2021
Accepted: May 28, 2021
Published: June 9, 2021

https://doi.org/10.1021/acs.est.1c01288
Environ. Sci. Technol. 2021, 55, 8742–8752

insights into both conditions.[32−34] However, the impact of incomplete mixing processes and non-Fickian dispersion on reaction kinetics is still not completely understood, especially in the third dimension (3D),[35] where the third dimension adds spatial heterogeneities to the system and greater tortuosities.[36] While some recent studies, both numerical and experimental, have addressed the complexity added by the third dimension on mixing and reactive processes,[22,37] and on mass transport between the stagnation zones and preferential paths,[38] our current understanding of flow dynamics and associated reactive processes in unsaturated porous media is very limited, owing to both the complexities associated with the presence of multiple phases and the difficulty in experimentally (in particular, optically) accessing these systems.

The development, over the past few decades, of noninvasive and nondestructive 3D imaging techniques at the pore scale opens a wide spectrum of possibilities to address the complexity of natural media, in which accessibility is limited.[22,39−41] To date, the use of techniques such as laser tomography, confocal microscopy, X-ray absorption computed tomography, or magnetic resonance imaging (MRI) has been limited to imaging the distribution of phases and multiphase flow,[42] fluid flow in saturated and unsaturated media,[41,43] conservative transport in saturated conditions,[22,44,45] and propagation of reactive waves.[39,46] For a detailed review of these noninvasive imaging methods, the reader is referred to Werth et al.[47] Some recent works have also demonstrated the capabilities of studying solute transport in unsaturated porous media at high temporal and spatial resolutions.[48] In this work, we employ MRI to visualize the 3D distribution of phases and reactants in unsaturated porous media.

The main goals of the present work are to measure pore-scale dynamics of local concentration to identify the mechanisms that control kinetics of transported reactions in unsaturated porous media and to systematically characterize the impact of phase saturation on the effective reaction rate of the system, i.e., on the product formation. For this purpose, we use an analogous porous medium consisting of glass beads and a catalyst/indicator reaction (mixing-limited bimolecular irreversible reaction). Two different glass bead sizes are used for the analysis, and several phase saturations and flow rates are explored. This experimental approach provides a completely new perspective for reactive transport in unsaturated porous media, and the experimental results are used to develop a theoretical framework in 3D based on the lamella mixing and reaction models by providing scaling laws for the effective reaction rate as a first step in the linking of the pore-scale phenomena to the Darcy (continuum) scale.

2. REACTIVE LAMELLA THEORY

2.1. Transport and Mixing. The transport at the pore scale of two initially segregated reactants is governed by advection, diffusion, and reaction. In the absence of inertial effects, the advection−reaction−diffusion equation can be used as the governing equation

$$\frac{\partial c_i}{\partial t} + \nabla\cdot(\boldsymbol{v}c_i) - D\nabla^2 c_i = r_i \tag{1}$$

where c_i is the concentration of the respective reactants, D is the molecular diffusion coefficient, $\boldsymbol{v}$ is the velocity field (calculated from the solution of the flow problem), and r_i is the local reaction rate. The heterogeneous velocity field, with complex streamline topologies, leads to the deformation of the interface between the displacing and the resident fluid. We refer to this as the mixing front. The deformation of the mixing front can enhance mixing and reaction rates by increasing the area available for diffusive mass transport.[24,29,30]

The lamella theory of mixing and reaction is a Lagrangian framework that considers the mixing front as a collection of numerous discretized elements that are referred to as lamellae. In 2D, the interface between two mixing fluids is a line that deforms, but in 3D, it is a planar structure (which is also referred to as a sheet).[49] This theory takes into account the deformation of the mixing interface via advection, which is quantified by the stretching rate γ and connects that to the mixing and reaction rates.[24−26] We consider an initially nondeformed interface involving a mixing-driven irreversible reaction A + B → P in a porous medium. At the pore scale, the deformation of the mixing interface of area ε, with initial area ε_0, is quantified by the elongation $\rho = \varepsilon/\varepsilon_0$[50] and its transport as[5,51,52]

$$\frac{\partial c_i}{\partial t} - \gamma n\frac{\partial c_i}{\partial t} - \frac{\partial}{\partial n}\left(D\frac{\partial c_i}{\partial n}\right) = r_i \tag{2}$$

where γ is defined as $\gamma = (1/\rho)(\mathrm{d}\rho/\mathrm{d}t)$ and n is the coordinate perpendicular to the lamella. Since the concentration gradients along lamella are small,[24] we assume that diffusive mass transfer is dominant only perpendicular to the lamella, i.e., along n.

The transport and reaction regimes are characterized by the dimensionless numbers Péclet (Pe) and Damköhler (Da), respectively. The Péclet number, $Pe = \tau_d/\tau_a = \overline{v}\xi/2D$, represents the ratio between the characteristic time of diffusion and the characteristic time of advection over a typical pore size ξ, $\overline{v}$ is the mean pore water velocity. The Damköhler number, $Da = \tau_a/\tau_r = \xi c_0\ k/\overline{v}$, represents the ratio of transport to reaction timescales. The characteristic reaction time, under well-mixed conditions, is calculated as $\tau_r = 1/c_0 k$, where k is the rate constant of our chosen reaction and c_0 is the initial concentration. When the reaction time scale is much smaller than the advection time scale, i.e., $Da \gg 1$, the reaction is driven by mixing.

2.2. Effective Reaction Rate: Mass of Product. For a fast irreversible reaction, in which the mass of A that diffuses from the interface into B reacts to produce P, the global kinetics, i.e., effective reaction rate R, of mass of product M_P over the interface Π can be written as[28,51]

$$R = \frac{\mathrm{d}M_P}{\mathrm{d}t} = D\int_\Pi |\nabla c_A|\mathrm{d}\varepsilon \approx \frac{Dc_0 S_w \varepsilon_0(1+\gamma t)}{s(t)} \tag{3}$$

where s is the width or transverse thickness of the interface (see Figure 1). It is assumed that $|\overline{\nabla c}| \sim c_0/s$. In natural systems, and in unsaturated soils in particular (with pore sizes $[1-10^{-4}]$ mm and pore flow velocities $[10^{-2}-10^{-6}]$ mm/s),[53] a shear flow regime is expected, in which the mixing front deforms by the gradient of velocity in the direction transverse to the main flow.[26] As detailed for 2D flows,[52,54] shear flows in 3D can also lead to a linear increase of elongation ($\rho = \nabla v t$) and a linear increase of the mixing interface area as $\varepsilon = S_w\varepsilon_0(1+\gamma t)$,[49] where S_w is the wetting saturation defined as the ratio of the volume occupied by the wetting phase (i.e., phase in which reaction is taking place) to that of the porous space. We estimate γ as $\overline{v}/\lambda = \overline{v}/(a/S_w)$, where λ is the velocity correlation length[55] and a is the pore throat (approximately one-fourth of the diameter of the beads[56]). λ increases as S_w

https://doi.org/10.1021/acs.est.1c01288
Environ. Sci. Technol. 2021, 55, 8742−8752

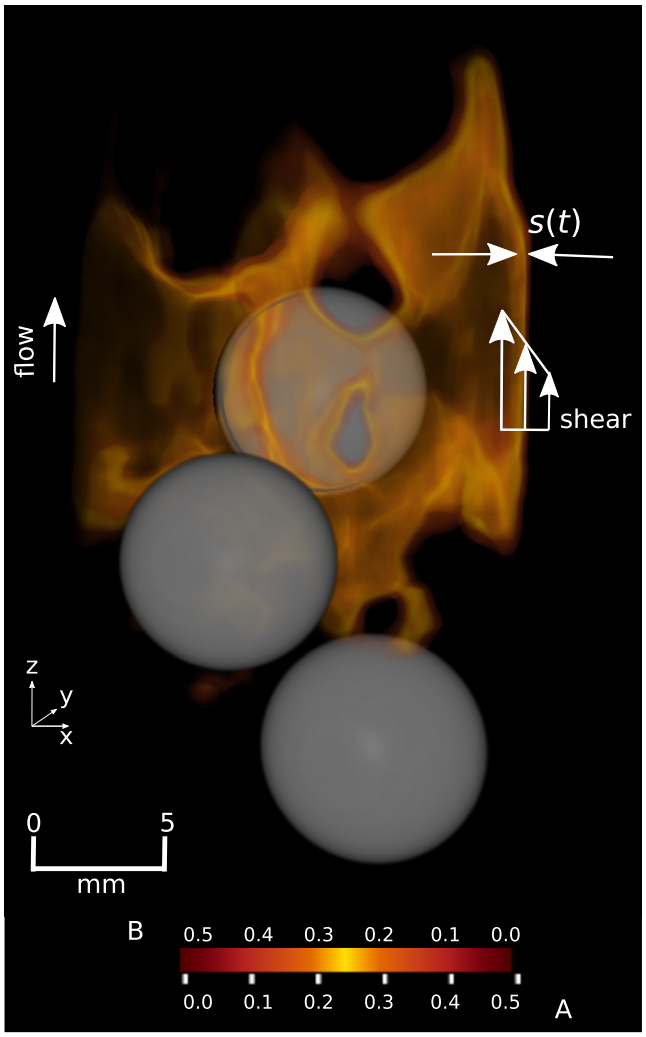

Figure 1. Experimental reconstruction of a 3D reactive lamella inside a fully saturated ($S_w = 1$) packed bed of 8 mm glass beads (only three beads in gray are shown for visualization simplicity). Concentration of the reactants within the mixing volume is shown in warm colors, in which the lightest color indicates equal concentrations of the invading (A) and resident (B) reactants. A is pumped into the porous medium at a constant flow rate ($Q = 0.252$ mm^3/s) from bottom to top. Shear is indicated with velocity vectors of different magnitudes. The width or transverse thickness of the lamella is labeled as $s(t)$. Note that the lamella shown is cut by an x−z (vertical) plane passing through the middle of the domain; beads are not cut by the plane (see the Supporting Information, Movie S1).

reduces as has been observed recently.[57,58] The elongation of the mixing front not only increases the area available for diffusive mass transport but also enhances the concentration gradients by compression normal to the surface. The competition between compression and molecular diffusion controls s as follows

$$s(t) = s_0\sqrt{\frac{3\beta - 2 + 2(1+\gamma t)^3}{3\beta(1+\gamma t)^2}} \quad (4)$$

where $\beta = s_0^2\gamma/D$ and s_0 is the initial interface thickness. When compression balances with diffusion, concentration gradients decrease and s grows diffusively as $s \sim t^{1/2}$. The time at which concentration gradients are maximum corresponds to the so-called mixing time $t_{mix} = \nabla v^{-1}\ (s_0^2\nabla v/D)^{1/3}$.[26,52,55] Note that the characteristic shear time, defined as $\tau_s = \nabla v^{-1}$, and the characteristic reaction time τ_r have been used to define the transition between different temporal scaling laws for R. Analytical expressions for these scaling laws have been derived for both weak ($Pe' < Da'$) and strong ($Pe' > Da'$) stretchings, with $Pe' = \tau_D/\tau_s$ and $Da' = \tau_D/\tau_r$, where $\tau_D = s_0^2/D$.[51] The different temporal scaling laws for the reaction rate R control the mass of product M_p. The mass is computed as $M_p(t) = \int_V c_p dx$ at instant t, where V is the total pore volume of the phase in which transport and reaction are happening.

2.3. Incomplete Mixing behind the Front. The incomplete mixing behind the reactive front makes the reaction persists locally in space and longer in time. The existence of concentration gradients mainly transverse to the main flow direction is responsible for the resilience in the system.[59] The decay of the concentration gradients and therefore of the reaction is mainly driven by the diffusion into the low-velocity regions or stagnation zones.[29,30] For a given position, i.e., a plane transverse to the main flow direction, after breakthrough of the reactive front, the reaction rate R decreases and can be scaled by a power law with an exponent, α.[60,61] This scaling is expected to be controlled not only by saturation S_w but also by Pe and Da.

3. MATERIALS AND METHODS

3.1. Porous Medium: Experimental Design. In this work, we consider a monodispersed 3D porous medium consisting of spherical grains (glass beads) contained in a cylindrical column of an internal diameter of 16 mm. Two different glass bead diameters (1 and 4 mm) are used, allowing to explore a wide range of experimental conditions. The column consists of a conical section at the bottom, a diffusing section, and a cylindrical section at the top, which represents our porous medium. Through the conical section, the injected liquid transitions from the diameter of the connecting pipe to the diameter of the cylindrical section. The height of the cone was designed with the help of computational fluid dynamics to minimize the boundary effects for the expected experimental flow rates (see Supporting Information, Figure S1). The diffusing section, composed of a fritted glass filter of 2 mm thickness and 500 μm pore size, is used to hold the beads and homogenize the flow of the invading reactant liquid (henceforth called A). It also acts as the limit between the invading and resident (henceforth called B) reactants during the experiment setup. The column is connected to a syringe pump (Harvard Apparatus PHD Ultra) to control the injection flow rate (Q) of injected reactant A. We control the syringe pump remotely using FlowControl software[62] (Figure 2).

As an immiscible nonwetting phase, a fluorinated hydrocarbon, tetrafluorohexane (C_6F_{14}, henceforth called O) is used for the unsaturated experiments. Tetrafluorohexane is a stable organic compound that does not react with any of the chemicals used (see Section 3.2) and is not miscible with water.

3.2. MRI: From Signal Intensity to Concentration. We chose a manganese reduction reaction to study the transport of the reaction front. A resident solution of Mn^{3+} ions (B) in the pore space is displaced by an invading solution containing Mn^{2+} (A) and reactant CHD. The reduction reaction consists of two steps (see eq 5a) and conversion from Mn^{3+} to Mn^{2+}.[63] The reacting solution used is H_2SO_4 (Sigma-Aldrich), 1,4-cyclohexanedione (CHD, Sigma-Aldrich), and manganese(III) acetate (Sigma-Aldrich)

https://doi.org/10.1021/acs.est.1c01288
Environ. Sci. Technol. 2021, 55, 8742−8752

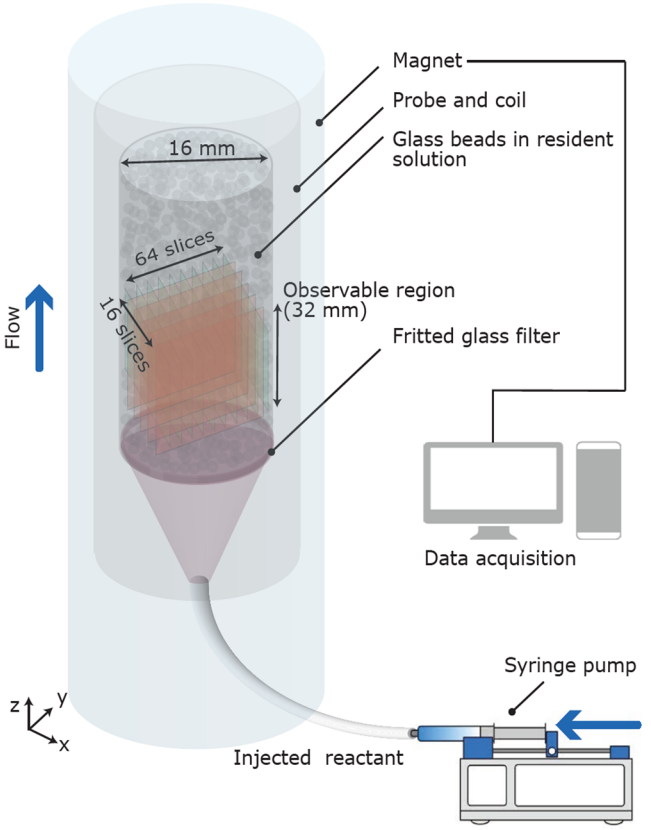

Figure 2. Scheme of the experimental setup. Glass beads are held within a glass cylinder by a fritted glass filter located at the bottom of the column. A syringe pump is used to inject reactant A at a constant flow rate into the column containing glass beads and reactant B. Flow sense is upward. The immiscible phase (O) for unsaturated experiments is allocated within the porous medium, accessing it from the upper part of the column. The porous medium column is placed inside the MRI magnet used for imaging the reaction. The visible field of view is 32 mm × 16 mm (vertical × horizontal).

$$2Mn^{3+} + CHD \rightarrow 2Mn^{2+} + H_2Q + 2H^+ \quad (5a)$$

$$2Mn^{3+} + H_2Q \rightarrow 2Mn^{2+} + Q + 2H^+ \quad (5b)$$

where H_2Q is an intermediate organic molecule, 1,4-hydroquinone, and Q is quinone. A solution of 0.5×10^{-3} M manganese(III) acetate initially filled the packed bed and a solution of 0.1 M CHD and 0.5×10^{-3} M manganese(II) acetate was injected into the packed bed. This ensures a constant total concentration of Mn ions (Mn^{2+} and Mn^{3+}), and that changes in signal intensity come from changes in the oxidative state of Mn^{3+}, rather than a depletion of manganese ions. All solutions were prepared in distilled, deionized water. These experiments were performed in high sulfuric acid conditions, which stabilizes Mn^{3+} ions in aqueous solutions.[64,65] We prepared fresh solutions before each experiment. The time scale of the reaction, which is visible optically, is calculated by a batch experiment. Using a CMOS camera, we first measure the time scale of dilution (without one of the reactants) and second the time scale of dilution+reaction. The difference between both times provides the reaction time scale, which is found to be $\tau_r \sim 1$ s (see Supporting Information, Figure S2).

MRI is the best technique to probe the concentration maps of manganese ions because there is poor optical contrast between the two oxidative states, particularly in a packed bed.[66−68] However, the nuclear magnetic resonance (NMR) signal intensity (I) depends on the concentration of manganese ions and their oxidative state (Mn^{2+} or Mn^{3+}).[66] There are more unpaired electrons in Mn^{2+} ions than Mn^{3+}, and as a result, the relaxation time for molecules surrounding Mn^{2+} is shorter. This produces the necessary contrast with which to visualize reactive fronts inside the porous medium using MRI. Therefore, initially, the nonwetting phase (O) and beads appear dark and resident Mn^{3+} (B) appears as the lighter phase. As the reaction occurs, the oxidative state of manganese ions changes, which in turn changes the visible intensity. Note that immiscible phase O does not contain protons and hence is visualized afterward.[69] The relaxation times (transverse or spin−spin relaxation times, $T_{2,m}$) for water can be converted into concentrations given that the total concentration of manganese ions remains constant ($[Mn]_0 = [Mn^{2+}] + [Mn^{3+}]$).[66]

$$\frac{1}{T_2} = k_x \quad (6)$$

$$\frac{1}{T_2} = \frac{1}{T_{2,Mn^{2+}}} + \frac{1}{T_{2,Mn^{3+}}} + \frac{1}{T_{2,beads}} \quad (7)$$

There is a simple linear relationship between the overall relaxation rate ($1/T_2$) of a paramagnetic species (m) and its concentration[63] (eq 6); however, it is also affected by the diamagnetic relaxation of the solvent and proximity to the glass beads (see the Supporting Information for details). The intensity observed is a combination of the total concentration

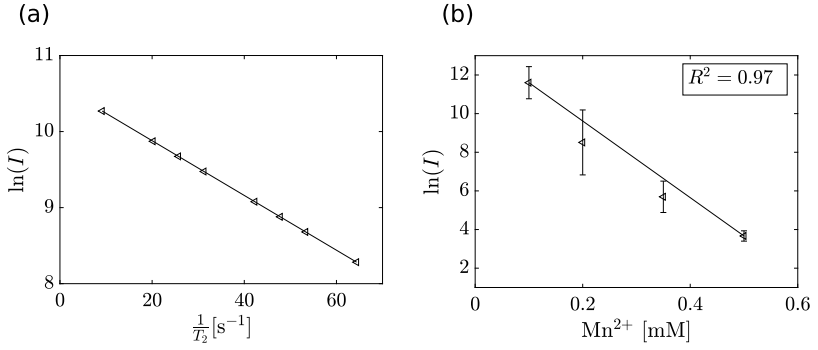

Figure 3. (a) Natural logarithm of the signal intensity (I) is proportional to the relaxation rate ($1/T_2$) (data from ref 66). (b) Natural logarithm of I against the concentration of Mn^{2+} in the experiments.

https://doi.org/10.1021/acs.est.1c01288
Environ. Sci. Technol. 2021, 55, 8742−8752

Table 1. Experimental Conditions of the Reactive Experiments in the Packed Beds of 1 and 4 mm Glass Beads (with Porosity ϕ = 0.3844 for 1 mm Glass Beads and ϕ = 0.4375 for 4 mm Glass Beads) for Different Saturation Degrees S_w[a]

1 mm grains					4 mm grains				
S_w	Q (mm^3/s)	$\overline{v}$ (mm/s)	Pe	Da	S_w	Q (mm^3/s)	$\overline{v}$ (mm/s)	Pe	Da
1.00	3.865	0.050	25	20	1.00	10.996	0.125	250	32
1.00	1.933	0.025	12.5	40	1.00	17.593	0.200	400	20
0.77	3.286	0.054	25	18	0.88	9.346	0.119	250	33
0.43	1.933	0.058	25	17	0.78	7.697	0.112	250	35

[a]Q is the imposed flow rate, $\overline{v}$ is the mean pore water velocity, Pe is the Péclet number, and Da is the Damköhler number.

of manganese ions [Mn] and the glass beads (eq 7). Calibration experiments were performed to quantify the contribution of glass beads by only measuring the relaxation time (and hence the intensity) for each of the individual species (m). The natural logarithm of intensity (I) is directly proportional to the relaxation rate ($1/T_2$)[63] (Figure 3a). This is correlated to the concentration of species, as shown in Figure 3b. For our calibration, the data follows a linear fit with a regression coefficient of R^2 = 0.97.

3.3. Experimental Protocol. The monodispersed 3D porous media were used to run saturated and unsaturated experiments at different flow rates Q. For the unsaturated experiments, the immiscible phase (O) to "desaturate" the system is injected from the upper side of the column, which was open (Figure 2). A syringe to control the volume and a needle were used to allocate O randomly (and homogeneously in the statistical sense) within the porous medium. Once the beads and resident chemicals (either B or B and O for saturated and unsaturated experiments, respectively) were placed inside the column, the latter was then carefully installed inside the magnet before the injection of A (Figure 2). Subsequently, the continuous injection of A was started. While for the saturated experiments, and in both porous media, two different flow rates (Q) were used; the flow rate in the unsaturated ones was modified to get similar Pe and Da to those in the saturated experiments for comparison. This modified flow rate is backcalculated using the same Pe as that of the fully saturated case. To ensure that there is no flow behavior missed between two consecutive scans, the upper limit of the imposed flow rate is determined by the acquisition time (16 s for a full 3D scan), i.e., the acquisition time must be longer than the advective time (τ_a). Owing to the capillary forces and low flow rates used, the immiscible phase was immobile during the course of the experiments, i.e., the magnitude of the viscous forces was smaller than the magnitude of capillary forces.[70] The capillary number Ca is estimated as $\mu_w Q\xi^2/(\sigma\kappa\varepsilon)$, where μ_w is the viscosity of the wetting phase (water), Q is the flow rate, σ is the surface tension between the two phases, and κ is the permeability. $Ca \approx 10^{-5}$ confirms that the O remains immobile. The saturation degrees (S_w), the flow rates imposed, the resulting mean pore water velocities ($\overline{v}$), and the Péclet (Pe) and Damköhler (Da) numbers experimented are summarized in Table 1.

1H and 19F magnetic resonance 3D images were acquired using a Bruker Avance III HD spectrometer that comprised a 7 T wide-bore superconducting magnet operating at a proton resonance frequency of 300.13 MHz. All images were acquired using a micro 2.5 imaging probe equipped with a dual resonance 1H/19F 25 mm radio frequency (RF) birdcage coil. The temperature of the imaging probe was maintained at 293 ± 0.3 K by the temperature of water-cooled gradient coils. Vertical (sagittal) 3D images of the system were acquired using the fast spin-echo imaging sequence RARE.[71] 1H 3D images were recorded using a 128 × 64 × 16 pixel matrix, with a field of view of 40 × 20 × 20 pixels. A RARE factor of 32, an echo time of 3.2 ms, and a repetition time of 500 ms were used. For each experiment, a series of images (from 20 to 100) were collected depending on the injection time. 3D 19F MR images were acquired to visualize the nonwetting phase O at t = 0 (before the injection of A) and at the end of the injection.[69] These 3D images were acquired using the same parameters as the 3D 1H MRI images, except for the repetition time, which was 1 s. Scans, at each time step, consisted of 16 slices (in the x direction), of 1 mm thickness, with a resolution of 0.25 mm (in the y and z directions). The size of each voxel is 0.25 mm× 0.25 mm× 1 mm, and thus, the voxel volume equal to 0.0625 mm^3. Signal intensity was stored in 16-bit grayscale images. All images were processed and then converted to images of concentration, averaging over the voxel size, using the calibration described above (Figure 3). Artifacts were corrected (see Supporting Information, Figure S3), and segmentation was used to differentiate the glass beads from the liquid phase. The segmented liquid volume is compared to the actual volume hosted in the porous medium. This action was also performed for the volume of the immiscible phase. The acquisition was carried out until no further reaction was detected in the visible domain. We compute for every time step the mass of Mn^{2+} injected and the excess mass visible in the pore volume as a consequence of reaction. The difference between these two provides the mass of Mn^{3+} that has reacted to produce Mn^{2+} in each voxel at every time step (see the Supporting Information, Figure S4). We then calculate the total mass of the product formed M_P as the sum in all voxels in the visible domain. The rate of change of M_P provides the effective reaction rate R.

4. RESULTS AND DISCUSSION

4.1. Flow and Saturation Control on the Dynamics of Reaction. Figure 4 shows the spatial distribution of the immiscible nonwetting phase O in the pore space of a porous medium built from 4 mm glass beads. Clusters of this phase connecting several pores and isolated drops can be recognized. The saturation of the wetting phase in this case is S_w = 0.78. O was immobile during the reactive transport experiment (for longitudinal S_w profiles, see Supporting Information Figure S5). For the same experiment, snapshots at six equispaced times of the concentration of the reactants within the mixing volume are shown in Figure 5, for an injection flow rate Q = 7.697 mm^3/s. Experimental conditions of the reactive experiments in both porous media (i.e., different glass beads diameter) are summarized in Table 1. As the invading chemical A enters the domain, it penetrates the channels created by the grains and O (see Figure 5). Initially, the

https://doi.org/10.1021/acs.est.1c01288
Environ. Sci. Technol. 2021, 55, 8742−8752

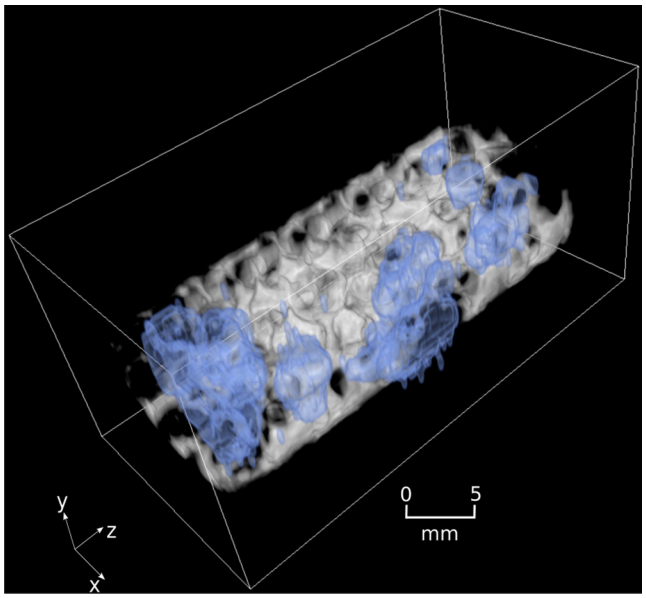

Figure 4. Distribution of resident reactant B (semitransparent white color) and immiscible nonwetting phase O (semitransparent blue color) within the monodispersed porous medium of 4 mm glass beads (nonvisible). The saturation of the wetting phase is S_w = 0.78. Controlled O volume was placed carefully and randomly using a needle in different parts of the column while taking care not to place a large volume in one particular location.

interface Π is highly stretched and due to heterogeneity of the pore space a collection of lamellar topological structures (or fingers) develops (Figure 5a–c). As the reaction propagates through the pore space, these fingers merge by diffusion and a more homogeneous reaction front propagates through the medium (Figure 5d). After breakthrough, incomplete mixing makes the reaction persist behind the front (Figure 5e,f) (see the Supporting Information, Movie S2).

As the chemicals react, we measure in time the effective reaction rate R and the mass of reaction product M_P for each experiment (symbols in Figure 6). For all our experiments, R initially increases. After breakthrough, R rapidly decreases and eventually the reaction dies out. For a given saturation, in this case, S_w = 1, a faster increase with time of R as flow rate increases, i.e., as Pe increases, is observed, irrespective of the grain size. For a given Pe, a lower magnitude of R as S_w decreases is observed (Figure 6a,b). The temporal evolution and magnitude of M_P follow the patterns dictated by R, although some features are better recognized as follows. In Figure 6c,d, it is seen that M_P for fully saturated cases depends on the Pe. A higher Pe leads to higher mass production. M_P for unsaturated cases reduces as S_w decreases. However, for 1 mm sized grains (Figure 6c), as S_w reduces to 0.77, the mass produced at the very early times is larger than in fully saturated conditions. This trend reverses when S_w reduces to 0.43, i.e., the rate of increase of M_P reduces as compared to S_w = 0.77. For low Pe (i.e., 1 mm sized grains), the rate of production of M_P decreases before the breakthrough (denoted by vertical lines in Figure 6c). On the contrary, for a higher Pe (i.e., 4 mm

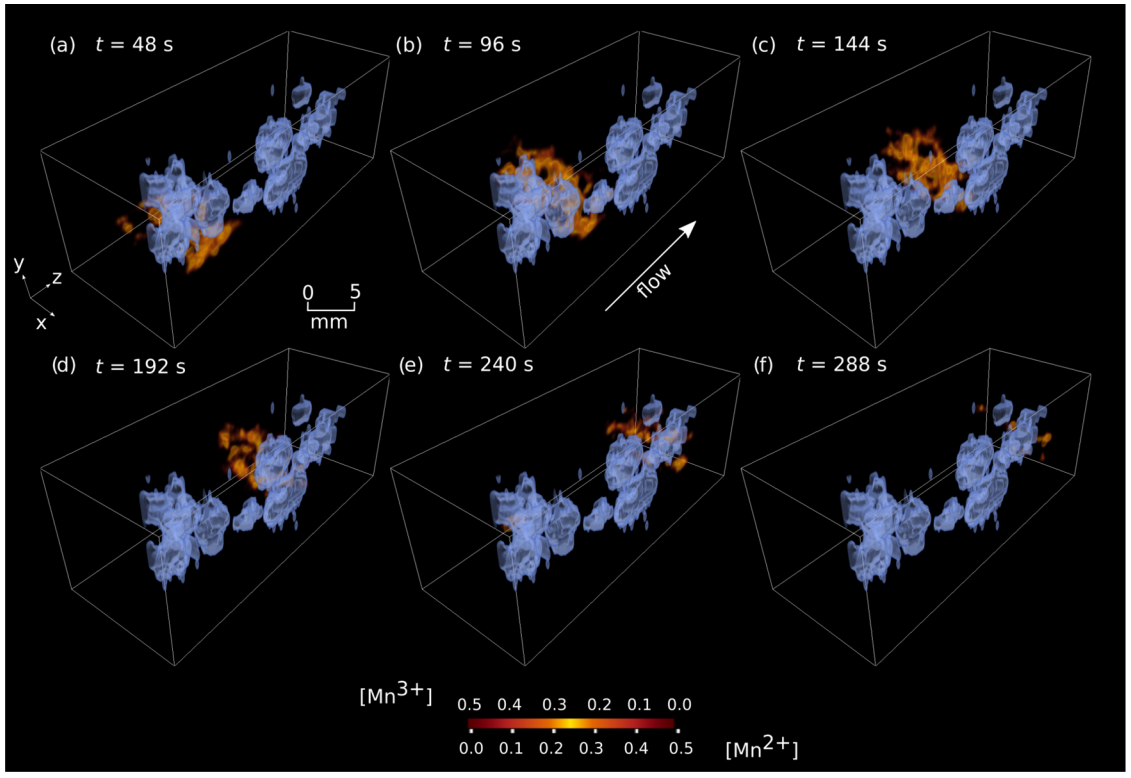

Figure 5. Time series of the transported reaction as A is pumped at a constant flow rate (Q = 7.697 mm^3/s) into an unsaturated packed bed of 4 mm glass beads. Concentration of the reactants within the mixing volume is shown in warm colors, in which the lightest color indicates equal concentrations of A and B (i.e., equal concentration of Mn^{2+} and Mn^{3+}, mM). Nonwetting phase O is shown in semitransparent blue color and does not move during the experiment. The saturation of the wetting phase is S_w = 0.78. Pe and Da numbers for this experiment are 250 and 35, respectively. The arrow denotes the mean flow direction. Images were acquired every 16 s (see the Supporting Information, Movie S2).

https://doi.org/10.1021/acs.est.1c01288
Environ. Sci. Technol. 2021, 55, 8742−8752

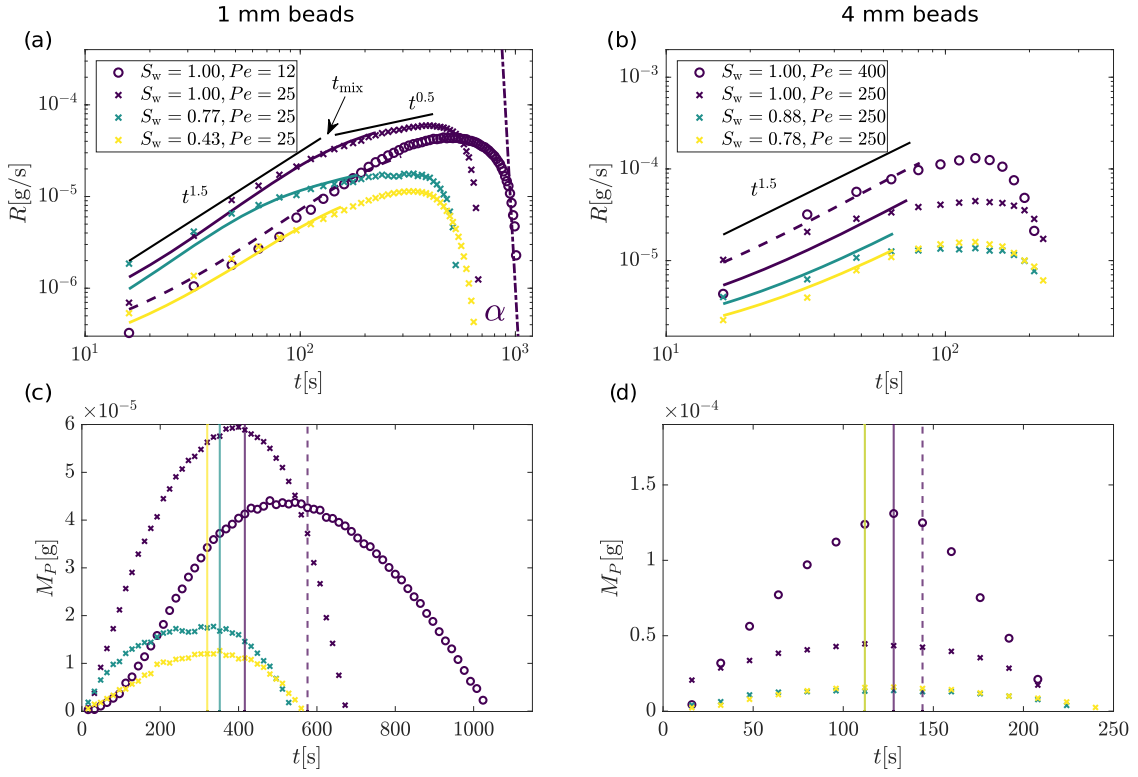

Figure 6. (a, b) Comparison of temporal evolution of the global reaction rate R for 1 and 4 mm sized grains, respectively, and different S_w values between the MRI experiment results (symbols) and the reactive lamella model (solid lines for the same Pe and dashed lines for a different Pe). Note that the same Pe is used for comparing different S_w values except where specified. The stretching ($t^{1.5}$) and the Fickian ($t^{0.5}$) regime are indicated with solid black lines. The mixing time (t_{mix}) between both regimes is also shown. The model prediction is shown until only breakthrough (i.e., the reaction front reaches the end of the observable domain). The dotted line in (a) depicts the speed α of reaction extinction after breakthrough. (c, d) Temporal evolution of M_P obtained from MRI experiments (symbols) for 1 and 4 mm sized beads, respectively, and different S_w values. Vertical lines denote when breakthrough happens.

Table 2. Parameters Used in Model Prediction[a]

1 mm grains							4 mm grains				
S_w	Pe	ε_0 (m^2)	s_0 (m)	γ (s^{-1})	t_{mix}^{exp} (s)	t_{mix}^{model} (s)	S_w	Pe	ε_0 (m^2)	s_0 (m)	γ (s^{-1})
1.00	12	0.0085	0.005	0.0626	208 ± 16	185	1.00	400	0.0616	0.005	0.1251
1.00	25	0.0085	0.005	0.1251	128 ± 16	116	1.00	250	0.0616	0.005	0.0782
0.77	25	0.0048	0.003	0.1059	110 ± 16	92	0.88	250	0.0547	0.005	0.0556
0.43	25	0.0037	0.003	0.0624		132	0.78	250	0.0481	0.005	0.0461

[a] s_0 and ε_0 are the initial interface thickness and area, respectively. γ is the shear deformation rate. t_{mix}^{model} is the mixing time computed from the lamella-based model and compared with the one inferred from the experiments. t_{mix}^{exp} is experimentally observed only for 1 mm sized grains since it is not reached in the 4 mm sized grains experiments. Uncertainty is added for t_{mix}^{exp} as the acquisition time (16 s).

sized grains), M_P production does not decrease before breakthrough (Figure 6d). After breakthrough, for both 1 and 4 mm sized grains, the rate of M_P production decreases slowly as saturation decreases (Figure 6c,d). Note that despite the differences between the measured porosities (0.3844 and 0.4375, for 1 and 4 mm sized grains, respectively), the maximum mass produced for S_w = 1 in 1 mm sized grains and Pe = 25 is M_P = 43.4 mg, whereas for the 4 mm sized grains and Pe = 250, it is M_P = 44.9 mg. Thus, the Pe and pore size play a key role in determining R and thus M_P.

4.2. Mixing Control on Reaction: Reactive Lamella Model Prediction. We now compare the results obtained from the experiments with the theoretical model presented in Section 2. We use the lamella model to describe the mixing interface as a collection of stretched lamellae and to predict the global reaction rate R as a function of S_w. The model parameters (s_0, ε_0, γ) used in eq 3 are given in Table 2. ε_0 is based on the geometry of the system and calculated as the area of the circle at the bottom of the column minus the area of the beads and O. γ is calculated as $\overline{v}/(a/S_w)$. s_0 cannot be measured by our apparatus and is therefore the only (manually) calibrated parameter. We assume that an initial width of 5 mm (and 3 mm for partially unsaturated cases of 1 mm beads) approximates well the initial width of the interface (note that the initial width roughly corresponds to the thickness of the fritted glass filter that initially separates both reactants, 2 mm). The solid lines in Figure 6a,b show the results of the model (only until breakthrough) and how they compare with the experimental observations (symbols).

At early times and for all S_w and Pe values, R grows in time faster than Fickian, i.e., $R \sim t^{1.5}$. In the temporal evolution of R for 1 mm sized grains, a change in the scaling from $t^{1.5}$ to $t^{0.5}$ for all S_w values before breakthrough is observed (Figure 6a). This change happens at time t_{mix} when diffusion overcomes

https://doi.org/10.1021/acs.est.1c01288
Environ. Sci. Technol. 2021, 55, 8742−8752

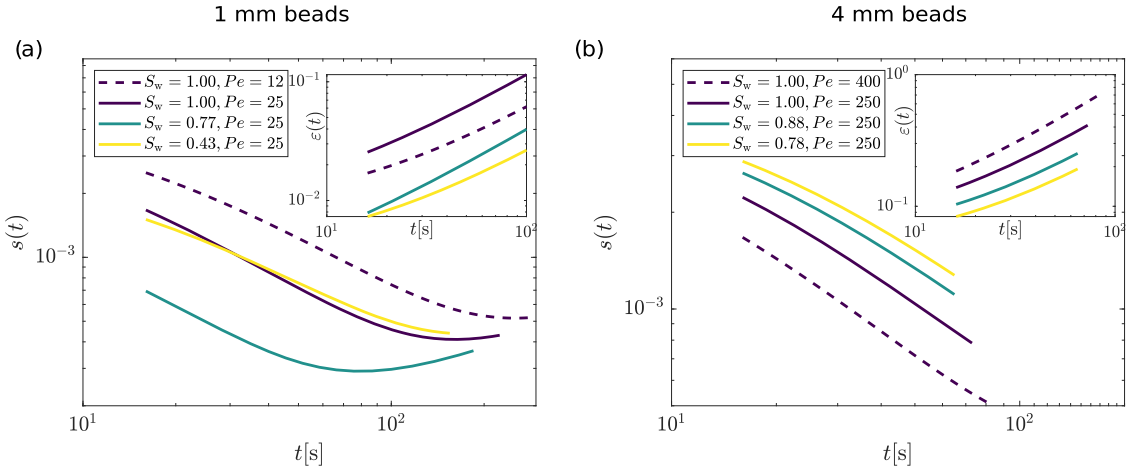

Figure 7. $s(t)$ and ε (inset) evolution computed from the reactive lamella model (eqs 2−4) for the time experiment before breakthrough in (a) 1 mm sized grains and (b) 4 mm sized grains.

compression and concentration gradients are no longer enhanced. At later times, folding of the plume over itself promotes lamellae interaction due to diffusion and they coalesce into bundles.[25] For 4 mm sized grains, the front breaks through before t_{mix} and the coalescence regime, thus no change in the scaling of R is observed (Figure 6b). After t_{mix}, ε no longer grows linearly[54] and the rate of product formation slows down. At longer times and for fully saturated conditions, R is expected to decay in time as Fickian (i.e., $R \sim t^{-0.5}$).[28] However, for unsaturated conditions, this decay is expected to be slower than Fickian and it would reduce as S_w decreases, as observed for 2D flows.[29,34] Comparing different S_w values (same Pe), t_{mix} is reached earlier at $S_w = 0.77$ than at $S_w = 1.00$, but a further reduction of S_w (i.e., 0.43) increases the mixing time (Figure 6a and Table 2). An analogy of this inversion in the trend can be found for conservative transport in unsaturated porous media, where a higher value of dispersivity and dispersion coefficient as saturation decreases is observed.[72,73] However, further observations indicate that this relation is not monotonic, and the maximum dispersivity and dispersion coefficient occur at intermediate saturation, called critical saturation.[74,75] While this has been explained by some authors for being the saturation where the tortuosity has its highest value, others argue the strong channeling effects in both fully saturated and low-saturation cases, being less significant at intermediate saturation values.[76]

The model overall gives a good agreement to our observations (until breakthrough). Hence, the assumption of linear stretching holds for spherical grains and the range of Pe used based on the fact the shear is induced by the velocity gradients between the no-slip boundary condition at the grain walls and the maximum velocity at the pore center.[77] We hypothesize this assumption is also valid in unsaturated conditions as shown below because the impact of the nonslip condition at the liquid−gas interfaces on transport processes has been recently demonstrated for being negligible.[78,79] For a given Pe, as S_w decreases, global reaction rate R can scale slightly higher than $t^{1.5}$ (Figure 6a). This can be explained by the temporal evolution of $s(t)$ and ε before breakthrough (Figure 7). For 1 mm sized grains, $s(t)$ decreases by compression until it reaches a minimum after which it grows diffusively. ε is the highest for $S_w = 1$, but slightly faster growth is observed for $S_w < 1$ due to a higher shear rate γ (Figure 7a). For the range of Pe and S_w explored, a constant gradient of velocity results from shear deformation, which is characterized by the transient mixing front strictly increasing linearly in time even for low S_w. According to Rolle and Le Borgne,[77] a strong stretching regime (i.e., $Pe' > Da'$) for the range of Pe and Da studied here is always experienced by the mixing and reactive front (Figure 7). We are able to characterize all of the results (for different Pe and S_w) using linear stretching ($\rho \sim t^1$). This also gives an insight into the permeability field of the domain: between a moderate and strong heterogeneity field.[25]

The reactive lamella model (eq 2) reduces to three parameters, s_0, ε_0, and γ, which can be evaluated as $\overline{v}/(a/S_w)$. Based on these estimations and without any other further fitting, the model provides a reasonable estimate of the global reaction rate in both fully and partially saturated conditions over the range of Pe investigated by taking into account the incomplete mixing at the pore scale.

4.3. Saturation Control on Reaction Extinction. Once breakthrough occurs, there is still a reaction happening within the system due to incomplete mixing.[23,80,81] As saturation decreases, it takes longer for the reaction to completely extinguish (see Figure 6). The presence of nonwetting phase O increases the volume fraction of the wetting fluid with low velocities, i.e., stagnation zone. This promotes further reaction with the creation of concentration gradients between the high-velocity regions or preferential paths and the low-velocity regions. In some cases, the consumption of the resident reactant can take place only by diffusion.[18,30] We define α as the rate of reaction extinction. As depicted in Figure 6, α is the slope of the reaction rate R tail calculated after breakthrough has already taken place. Figure 8 compares α for both grain sizes and all Pe values studied. α increases as S_w decreases. For $S_w = 1$, increasing Pe (more than an order of magnitude, from 25 to 250) does not increase α by the same amount (Figure 8). When $S_w < 1$, α increases by a similar order of magnitude independently of the Pe. Thus, a higher Pe does not necessarily lead to an increase in resilience of the reaction; it is in fact S_w that is the main controller of how long a reaction lasts inside the pore space.

We have demonstrated and quantified experimentally the incomplete mixing at pore scale in 3D porous media and the impact of the presence of an immiscible phase on it. The mixing and reactive front have been depicted by a lamella-like

https://doi.org/10.1021/acs.est.1c01288
Environ. Sci. Technol. 2021, 55, 8742−8752

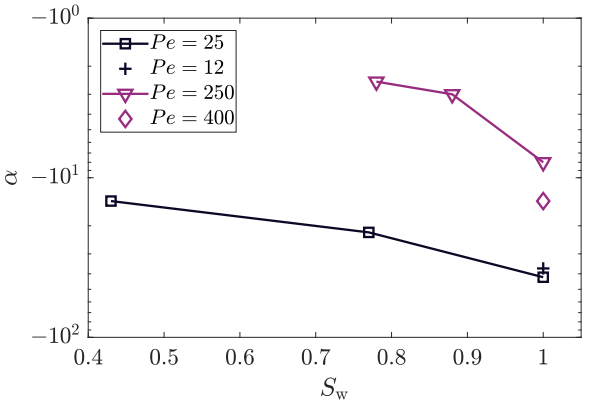

Figure 8. Impact of S_w on reaction extinction after breakthrough for different grain sizes and P: 4 mm sized grains, Pe = 250 and 400, purple symbols; 1 mm sized grains, Pe = 25 and 12, black symbols.

topology. The front is advected and deformed by the heterogeneous velocity field, being subjected to stretching and folding, resulting in a competition between compression (creation of concentration gradients) and diffusion (destruction of concentration gradients). Compared to the 2D case,[28] we get a more stretched 3D reaction front, and an enhanced reaction is expected due to the presence of helical flow components and transverse mixing.[82−84] However, the mechanisms that control the dynamics remain the same, having a similar temporal scaling for the stretching regime ($R \sim t^{1.5}$) and after the mixing time ($R \sim t^{0.5}$) under shear flows and strong stretching conditions.[77] This is the first time in our knowledge that the lamella-based theory is used for reactive transport in partially saturated porous media in 3D and has been successfully validated. At the scale of applications, although the fringes of the plumes are considered reaction hotspots,[85−87] subsurface environments are in general poorly mixed.[88] For instance, the initial response (at early times) can be crucial in understanding biogeochemical processes in unsaturated soils. While we considered a fast reaction compared to the transport in a small domain, such reactions are relatively common in natural environments.[89] These findings have implications for the understanding and upscaling of reactive transport in a variety of applications.

■ ASSOCIATED CONTENT

Supporting Information

The Supporting Information is available free of charge at https://pubs.acs.org/doi/10.1021/acs.est.1c01288.

CFD simulation of column design; reaction time scale from the batch experiment; artifacts correction, and mass of reaction product calculation; and longitudinal saturation profiles (PDF)

Propagation of reaction front inside the pore space of 8 mm sized glass beads (Movie_S1) (MP4)

Propagation of reaction front (and incomplete mixing after breakthrough) in the pore space of an unsaturated 4 mm sized glass beads (Movie_S2) (MP4)

■ AUTHOR INFORMATION

Corresponding Author

Joaquín Jiménez-Martínez − *Eawag, Swiss Federal Institute of Aquatic Science and Technology, 8600 Dübendorf, Switzerland; Department of Civil, Environmental and Geomatic Engineering, ETH Zürich, 8093 Zürich, Switzerland;* orcid.org/0000-0002-2063-6490; Email: joaquin.jimenez@eawag.ch, jjimenez@ethz.ch

Authors

Ishaan Markale − *Eawag, Swiss Federal Institute of Aquatic Science and Technology, 8600 Dübendorf, Switzerland; Department of Civil, Environmental and Geomatic Engineering, ETH Zürich, 8093 Zürich, Switzerland;* orcid.org/0000-0002-1370-8062

Gabriele M. Cimmarusti − *School of Chemistry, University of Birmingham, Birmingham B15 2TT, U.K.*

Melanie M. Britton − *School of Chemistry, University of Birmingham, Birmingham B15 2TT, U.K.*

Complete contact information is available at: https://pubs.acs.org/10.1021/acs.est.1c01288

Notes

The authors declare no competing financial interest.

■ ACKNOWLEDGMENTS

I.M. and J.J.-M. acknowledge the financial support from the Swiss National Science Foundation (SNF, grant Nr. 200021_178986). M.M.B. and G.M.C. acknowledge the financial support from the University of Birmingham and the Engineering and Physical Science (EPSRC) Research Council, U.K. (EP/K039245/1). The authors thank Dr. V. Niasar and two anonymous reviewers whose valuable comments and suggestions help to improve the manuscript. The authors also acknowledge Dr. T. Le Borgne for the constructive discussions.

■ REFERENCES

(1) De Simoni, M.; Carrera, J.; Sanchez-Vila, A.; Guadagnini, A. A procedure for the solution of multicomponentreactive transport problems *Water Resour. Res.* 2005, *41*, W11410 DOI: 10.1029/2005WR004056.

(2) Tartakovsky, A. M.; Redden, G.; Lichtner, P. C.; Scheibe, T. D.; Meakin, P. Mixing-induced precipitation: Experimental study and multiscale numerical analysis. *Water Resour. Res.* **2008**, *44*, No. W06S04.

(3) Rezaei, M.; Sanz, E.; Raeisi, E.; Ayora, C.; Vázquez-Suñé, E.; Carrera, J. Reactive transport modeling of calcite dissolution in the fresh-salt water mixing zone. *J. Hydrol.* **2005**, *311*, 282−298.

(4) Ottino, J. *The Kinematics of Mixing: Stretching, Chaos, and Transport*; Cambridge University Press, 1989.

(5) Ranz, W. E. Applications of a stretch model to mixing, diffusion, and reaction in laminar and turbulent flows. *AIChE J.* **1979**, *25*, 41−47.

(6) Villermaux, E.; Duplat, J. Mixing as an aggregation process. *Phys. Rev. Lett.* **2003**, *91*, No. 184501.

(7) Duplat, J.; Villermaux, E. Mixing by random stirring in confined mixtures. *J. Fluid Mech.* **2008**, *617*, 51−86.

(8) Jiménez-Martínez, J.; Negre, C. F. A. Eigenvector centrality for geometric and topological characterization of porous media. *Phys. Rev. E* **2017**, *96*, No. 013310.

(9) Xu, L.; Baldocchi, D. D.; Tang, J. How soil moisture, rain pulses, and growth alter the response of ecosystem respiration to temperature. *Global Biogeochem. Cycles* **2004**, *18*, No. GB4002.

(10) Giardina, C. P.; Litton, C. M.; Crow, G. P.; Susan, E. and Asner Warming-related increases in soil CO_2 efflux are explained by increased below-ground carbon flux. *Nat. Clim. Change* **2014**, *4*, 822−847.

(11) Ebrahimi, A.; Or, D. Dynamics of soil biogeochemical gas emissions shaped by remolded aggregate sizes and carbon configurations under hydration cycles. *Global Change Biol.* **2018**, *24*, e378−e392.

(12) Sebilo, M.; Mayer, B.; Nicolardot, B.; Pinay, G.; Mariotti, A. Long-term fate of nitrate fertilizer in agricultural soils. *Proc. Natl. Acad. Sci. U.S.A.* **2013**, *110*, 18185−18189.
(13) Helton, A. M.; Ardón, M.; Bernhardt, E. S. Thermodynamic constraints on the utility of ecological stoichiometry for explaining global biogeochemical patterns. *Ecol. Lett.* **2015**, *18*, 1049−1056.
(14) Kravchenko, A. N.; Toosi, E. R.; Guber, A. K.; Ostrom, N. E.; Yu, J.; Azeem, K.; Rivers, M. L.; Robertson, G. P. Hotspots of soil N_2O emission enhanced through water absorption by plant residue. *Nat. Geosci.* **2017**, *10*, 496−500.
(15) Winkel, L.; Vriens, B.; Jones, G.; Schneider, L.; Pilon-Smits, E.; Bañuelos, G. Selenium cycling across soil-plant-atmosphere interfaces: a critical review. *Nutrients* **2015**, *7*, 4199−4239.
(16) Duduković, M. P.; Larachi, F.; Mills, P. L. Multiphase catalytic reactors: a perspective on current knowledge and future trends. *Catal. Rev.* **2002**, *44*, 123−246.
(17) Rolle, M.; Eberhardt, C.; Chiogna, G.; Cirpka, O. A.; Grathwohl, P. Enhancement of dilution and transverse reactive mixing in porous media: Experiments and model-based interpretation. *J. Contam. Hydrol.* **2009**, *110*, 130−142.
(18) Jiménez-Martínez, J.; Porter, M. L.; Hyman, J. D.; Carey, J. W.; Viswanathan, H. S. Mixing in a three-phase system: Enhanced production of oil-wet reservoirs by CO_2 injection. *Geophys. Res. Lett.* **2016**, *43*, 196−205.
(19) Winogard, I. J. Radioactive waste disposal in thick unsaturated zones. *Science* **1981**, *212*, 1457−1464.
(20) Šimůnek, J.; van Genuchten, M. T. Modeling nonequilibrium flow and transport processes using HYDRUS. *Vadose Zone J.* **2008**, *7*, 782.
(21) Williams, K. H.; Kemna, A.; Wilkins, M. J.; Druhan, J.; Arntzen, E.; N'Guessan, A. L.; Long, P. E.; Hubbard, S. S.; Banfield, J. F. Geophysical monitoring of coupled microbial and geochemical processes during stimulated subsurface bioremediation. *Environ. Sci. Technol.* **2009**, *43*, 6717−6723. PMID: 19764240.
(22) Heyman, J.; Lester, D. R.; Turuban, R.; Méheust, Y.; Le Borgne, T. Stretching and folding sustain microscale chemical gradients in porous media. *Proc. Natl. Acad. Sci. U.S.A.* **2020**, *117*, 13359−13365.
(23) Wright, E. E.; Richter, D. H.; Bolster, D. Effects of incomplete mixing on reactive transport in flows through heterogeneous porous media. *Phys. Rev. Fluids* **2017**, *2*, No. 114501.
(24) Borgne, T. L.; Ginn, T. R.; Dentz, M. Impact of fluid deformation on mixing-induced chemical reactions in heterogeneous flows. *Geophys. Res. Lett.* **2014**, *41*, 7898−7906.
(25) Le Borgne, T.; Dentz, M.; Villermaux, E. Stretching, coalescence, and mixing in porous media. *Phys. Rev. Lett.* **2013**, *110*, 1−5.
(26) Le Borgne, T.; Dentz, M.; Villermaux, E. The lamellar description of mixing in porous media. *J. Fluid Mech.* **2015**, *770*, 458−498.
(27) Lester, D. R.; Dentz, M.; Le Borgne, T. Chaotic mixing in three-dimensional porous media. *J. Fluid Mech.* **2016**, *803*, 144−174.
(28) Anna, P.; Jiménez-Martínez, J.; Tabuteau, H.; Turuban, R.; Le Borgne, T.; Derrien, M.; Méheust, Y. Mixing and reaction kinetics in porous media: An experimental pore scale quantification. *Environ. Sci. Technol.* **2014**, *48*, 508−516.
(29) Jiménez-Martínez, J.; de Anna, P.; Tabuteau, H.; Turuban, R.; Le Borgne, T.; Méheust, Y. Pore-scale mechanisms for the enhancement of mixing in unsaturated porous media and implications for chemical reactions. *Geophys. Res. Lett.* **2015**, *42*, 5316−5324.
(30) Jiménez-Martínez, J.; Le Borgne, T.; Tabuteau, H.; Méheust, Y. Impact of saturation on dispersion and mixing in porous media: Photobleaching pulse injection experiments and shear-enhanced mixing model. *Water Resour. Res.* **2017**, *53*, 1457−1472.
(31) Karadimitriou, N. K.; Joekar-Niasar, V.; Babaei, M.; Shore, C. A. Critical role of the immobile zone in non-Fickian two-phase transport: A new paradigm. *Environ. Sci. Technol.* **2016**, *50*, 4384−4392.
(32) Willingham, T.; Werth, C.; Valocchi, A. Evaluation of the effects of porous media structure on mixing-controlled reactions using pore-scale modeling and micromodel experiments. *Environ. Sci. Technol.* **2008**, *42*, 3185−3193.
(33) Li, P.; Berkowitz, B. Characterization of mixing and reaction between chemical species during cycles of drainage and imbibition in porous media. *Adv. Water Resour.* **2019**, *130*, 113−128.
(34) Jiménez-Martínez, J.; Alcolea, A.; Straubhaar, J. A.; Renard, P. Impact of phases distribution on mixing and reactions in unsaturated porous media. *Adv. Water Resour.* **2020**, *144*, No. 103697.
(35) Dentz, M.; Le Borgne, T.; Englert, A.; B, B. Mixing, spreading and reaction in heterogeneous media: A brief review. *J. Contam. Hydrol.* **2011**, *120*−*121*, 1−17.
(36) Ghanbarian, B.; Hunt, A. G.; Ewing, R. P.; Sahimi, M. Tortuosity in porous media: A critical review. *Soil Sci. Soc. Am. J.* **2013**, *77*, 1461.
(37) Comolli, A.; De Wit, A.; Brau, F. Dynamics of $A + B \rightarrow C$ reaction fronts under radial advection in three dimensions. *Phys. Rev. E* **2019**, *100*, No. 052213.
(38) Hasan, S.; Joekar-Niasar, V.; Karadimitriou, N. K.; Sahimi, M. Saturation Dependence of Non-Fickian Transport in Porous Media. *Water Resour. Res.* **2019**, *55*, 1153−1166.
(39) Britton, M.; Sederman, A.; Taylor, A.; Scott, S.; Gladden, L. Magnetic resonance imaging of flow-distributed oscillations. *J. Phys. Chem. A* **2005**, *109*, 8306−8313.
(40) Wildenschild, D.; Vaz, C.; Rivers, M.; Rikard, D.; Christensen, B. Using X-ray computed tomography in hydrology: systems, resolutions, and limitations. *J. Hydrol.* **2002**, *267*, 285−297.
(41) Krummel, A. T.; Datta, S. S.; Münster, S.; Weitz, D. A. Visualizing multiphase flow and trapped fluid configurations in a model three-dimensional porous medium. *AIChE J.* **2013**, *59*, 1022−1029.
(42) Berg, S.; Ott, H.; Klapp, S. A.; Schwing, A.; Neiteler, R.; Brussee, N.; Makurat, A.; Leu, L.; Enzmann, F.; Schwarz, J.-O.; Kersten, M.; Irvine, S.; Stampanoni, M. Real-time 3D imaging of Haines jumps in porous media flow. *Proc. Natl. Acad. Sci. U.S.A.* **2013**, *110*, 3755−3759.
(43) Deurer, M.; Vogeler, I.; Khrapichev, A.; Scotter, D. Imaging of water flow in porous media by magnetic resonance imaging microscopy. *J. Environ. Qual.* **2002**, *31*, 487−493.
(44) Greiner, A.; Schreiber, W.; Brix, G.; Kinzelbach, W. Magnetic resonance imaging of paramagnetic tracers in porous media: Quantification of flow and transport parameters. *Water Resour. Res.* **1997**, *33*, 1461−1473.
(45) Pearl, Z.; Magaritz, M.; Bendel, P. Nuclear Magnetic Resonance Imaging of Miscible Fingering in Porous Media. *Transp. Porous Media* **1993**, *12*, 107−123.
(46) Rose, H. E.; Britton, M. M. Magnetic resonance imaging of reaction-driven viscous fingering in a packed bed. *Microporous Mesoporous Mater.* **2013**, *178*, 64−68.
(47) Werth, C. J.; Zhang, C.; Brusseau, M. L.; Oostrom, M.; Baumann, T. A review of non-invasive imaging methods and applications in contaminant hydrogeology research. *J. Contam. Hydrol.* **2010**, *113*, 1−24.
(48) Hasan, S.; Niasar, V.; Karadimitriou, N. K.; Godinho, J. R. A.; Vo, N. T.; An, S.; Rabbani, A.; Steeb, H. Direct characterization of solute transport in unsaturated porous media using fast X-ray synchrotron microtomography. *Proc. Natl. Acad. Sci. U.S.A.* **2020**, *117*, 23443−23449.
(49) Martínez-Ruiz, D.; Meunier, P.; Favier, B.; Duchemin, L.; Villermaux, E. The diffusive sheet method for scalar mixing. *J. Fluid Mech.* **2018**, *837*, 230−257.
(50) Meunier, P.; Villermaux, E. The diffusive strip method for scalar mixing in two dimensions. *J. Fluid Mech.* **2010**, *662*, 134−172.
(51) Bandopadhyay, A.; Le Borgne, T.; Méheust, Y.; Dentz, M. Enhanced reaction kinetics and reactive mixing scale dynamics in mixing fronts under shear flow for arbitrary Damköhler numbers. *Adv. Water Resour.* **2017**, *100*, 78−95.

https://doi.org/10.1021/acs.est.1c01288
Environ. Sci. Technol. 2021, 55, 8742−8752

(52) Bandopadhyay, A.; Davy, P.; Le Borgne, T. Shear flows accelerate mixing dynamics in hyporheic zones and hillslopes. *Geophys. Res. Lett.* **2018**, *45*, 11659−11668.
(53) Vanderborght, J.; Vereecken, H. Review of dispersivities for transport modeling in soils. *Vadose Zone J.* **2007**, *6*, 29−52.
(54) De Anna, P.; Dentz, M.; Tartakovsky, A.; Le Borgne, T. The filamentary structure of mixing fronts and its control on reaction kinetics in porous media flows. *Geophys. Res. Lett.* **2014**, *41*, 4586−4593.
(55) Villermaux, E. Mixing by porous media. *C. R. Mec.* **2012**, *340*, 933−943.
(56) Glover, P. W.; Déry, N. Streaming potential coupling coefficient of quartz glass bead packs: Dependence on grain diameter, pore size, and pore throat radius. *Geophysics* **2010**, *75*, F225−F241.
(57) Velásquez-Parra, A.; Tomás, A.; Willmann, M.; Méheust, Y.; Le Borgne, T.; Jiménez-Martínez, J. Sharp transition to strongly anomalous transport in unsaturated porous media. arXiv:2103.08016, arXiv.org e-Print archive, https://arxiv.org/abs/2103.08016 (submitted Mar 14, 2021).
(58) An, S.; Hasan, S.; Erfani, H.; Babaei, M.; Niasar, V. Unravelling effects of the pore-size correlation length on the two-phase flow and solute transport properties: GPU-based pore-network modeling. *Water Resour. Res.* **2020**, *56*, No. e2020WR027403.
(59) Meunier, P.; Villermaux, E. How vortices mix. *J. Fluid Mech.* **2003**, *476*, 213−222.
(60) Dentz, M.; Icardi, M.; Hidalgo, J. J. Mechanisms of dispersion in a porous medium. *J. Fluid Mech.* **2018**, *841*, 851−882.
(61) Nissan, A.; Alcolombri, U.; de Schaetzen, F.; Berkowitz, B.; Jimenez-Martinez, J. Reactive transport with fluid-solid interactions in dual-porosity media. *ACS ES&T Water* **2020**, *1*, 259−268.
(62) FlowControl. https://www.harvardapparatus.com/pumps-liquid-handling/software.html. 2002
(63) Britton, M. M. Measurement of the concentration of Mn^{2+} and Mn^{3+} in the Manganese-Catalyzed 1,4-Cyclohexanedione/Acid/Bromate reaction using redox-triggered Magnetic Resonance Spectroscopy. *J. Phys. Chem. A* **2006**, *110*, 13209−13214.
(64) Cotton, F. A.; Wilkinson, G.; Murillo, C. A.; Bochmann, M. *Advanced Inorganic Chemistry*, 6th ed.; Wiley, 1999.
(65) Kluh, I.; Doležal, J.; Zyká, J. Rasche reduktometrische Bestimmung von Mangan in Legierungen und Mineralien. *Fresenius' Z. Anal. Chem.* **1924**, *177*, 14−20.
(66) Britton, M. M. Spatial quantification of Mn^{2+} and Mn^{3+} concentrations in the Mn-catalyzed 1,4-Cyclohexanedione/Acid/Bromate reaction using magnetic resonance Imaging. *J. Phys. Chem. A* **2006**, *110*, 2579−2582.
(67) Britton, M. M. MRI of chemical reactions and processes. *Prog. Nucl. Magn. Reson. Spectrosc.* **2017**, *101*, 51−70.
(68) Britton, M. M. Magnetic resonance imaging of chemistry. *Chem. Soc. Rev.* **2010**, *39*, 4036−4043.
(69) Ramskill, N.; Bush, I.; Sederman, A.; Mantle, M.; Benning, M.; Anger, B.; Appel, M.; Gladden, L. Fast imaging of laboratory core floods using 3D compressed sensing RARE MRI. *J. Magn. Reson.* **2016**, *270*, 187−197.
(70) Tang, J.; Smit, M.; Vincent-Bonnieu, S.; Rossen, W. R. New capillary number definition for micromodels: The impact of pore microstructure. *Water Resour. Res.* **2019**, *55*, 1167−1178.
(71) Hennig, J.; Nauerth, A.; Friedburg, H. RARE imaging: A fast imaging method for clinical MR. Magnetic resonance in medicine. *Magn. Reson. Med.* **1986**, *3*, 823−833.
(72) Muller, K. A.; Ramsburg, C. A. Influence of nonwetting phase saturation on dispersivity in laboratory-scale sandy porous media. *Environ. Eng. Sci.* **2018**, *35*, 1062−1074.
(73) Matsubayashi, U.; Devkota, L. P.; Takagi, F. Characteristics of the dispersion coefficient in miscible displacement through a glass beads medium. *J. Hydrol.* **1997**, *192*, 51−64.
(74) Toride, N.; Inoue, M.; Leij, F. J. Hydrodynamic dispersion in an unsaturated dune sand. *Soil Sci. Soc. Am. J.* **2003**, *67*, 703−712.
(75) Raoof, A.; Hassanizadeh, S. M. Saturation-dependent solute dispersivity in porous media: Pore-scale processes. *Water Resour. Res.* **2013**, *49*, 1943−1951.
(76) Birkholzer, J.; Tsang, C.-F. Solute channeling in unsaturated heterogeneous porous media. *Water Resour. Res.* **1997**, *33*, 2221−2238.
(77) Rolle, M.; Le Borgne, T. Mixing and reactive fronts in the subsurface. *Rev. Mineral. Geochem.* **2019**, *85*, 111−142.
(78) Guédon, G. R.; Inzoli, F.; Riva, M.; Guadagnini, A. Pore-scale velocities in three-dimensional porous materials with trapped immiscible fluid. *Phys. Rev. E* **2019**, *100*, No. 043101.
(79) Triadis, D.; Jiang, F.; Bolster, D. Anomalous dispersion in pore-scale simulations of two-phase flow. *Transp. Porous Media* **2019**, *126*, 337−353.
(80) Le Borgne, T.; Dentz, M.; Davy, P.; Bolster, D.; Carrera, J.; de Dreuzy, J.-R.; Bour, O. Persistence of incomplete mixing: A key to anomalous transport. *Phys. Rev. E* **2011**, *84*, No. 015301.
(81) Valocchi, A.; Bolster, D.; Werth, C. Mixing-Limited Reactions in Porous Media. *Transp. Porous Media* **2019**, *130*, 157−182.
(82) Cirpka, O. A.; Chiogna, G.; Rolle, M.; Bellin, A. Transverse mixing in three-dimensional nonstationary anisotropic heterogeneous porous media. *Water Resour. Res.* **2015**, *51*, 241−260.
(83) Ye, Y.; Chiogna, G.; Cirpka, O. A.; Grathwohl, P.; Rolle, M. Experimental investigation of transverse mixing in porous media under helical flow conditions. *Phys. Rev. E* **2016**, *94*, No. 013113.
(84) Ye, Y.; Chiogna, G.; Lu, C.; Rolle, M. Effect of anisotropy structure on plume entropy and reactive mixing in helical flows. *Transp. Porous Media* **2018**, *121*, 315−322.
(85) McClain, M. E.; Boyer, E. W.; Dent, C. L.; Gergel, S. E.; Grimm, N. B.; Groffman, P. M.; Hart, S. C.; Harvey, J. W.; Johnston, C. A.; Mayorga, E.; McDowell, W. H.; Pinay, G. Biogeochemical hot spots and hot moments at the interface of terrestrial and aquatic ecosystems. *Ecosystems* **2003**, *6*, 301−312.
(86) Stegen, J. C.; Fredrickson, J. K.; Wilkins, M. J.; Konopka, A. E.; Nelson, W. C.; Arntzen, E. V.; Chrisler, W. B.; Chu, R. K.; Danczak, R. E.; Fansler, S. J.; Kennedy, D. W.; Resch, C. T.; Tfaily, M. Groundwater-surface water mixing shifts ecological assembly processes and stimulates organic carbon turnover. *Nat. Commun.* **2016**, *7*, No. 11237.
(87) Pool, M.; Dentz, M. Effects of heterogeneity, connectivity, and density variations on mixing and chemical reactions under temporally fluctuating flow conditions and the formation of reaction patterns. *Water Resour. Res.* **2018**, *54*, 186−204.
(88) Kitanidis, P.; McCarty, P. Delivery and Mixing in the Subsurface: Processes and Design Principles for In Situ Remediation. In *SERDP/ESTCP Environmental Remediation Technology*, 1st ed.; Springer, 2012; Vol. *4*.
(89) Sparks, D. L. *Kinetics of Soil Chemical Processes*; Academic Press, 2013.

https://doi.org/10.1021/acs.est.1c01288
Environ. Sci. Technol. 2021, 55, 8742−8752